

Supporting Information

FeS₂ deposited on 3D-printed carbon microlattices as free-standing electrodes for lithium-ion batteries

Cameron Romero,^a Zhi Liu,^a Kenneth Gordon,^a Xiaobo Lei,^b Karius Joseph,^a Emily Broussard,^a
Daniel Gang,^b Zhen Wei,^a and Ling Fei^{*a}

^a Department of Chemical Engineering, University of Louisiana at Lafayette, Lafayette, LA 70504, USA.

^b Department of Civil Engineering, University of Louisiana at Lafayette, Lafayette, LA 70504, USA.

Experimental Section

Structural Preparation

The microlattices were drawn using SolidWorks. First, a cube with an edge length of 533 μm was drawn. Then, on one of each of the parallel planes, a centered square with a side length of 267 μm was added and an extruded cut was performed. This process made the unit cell of the microlattice. The unit cell was then repeated 25 times in both the x and y-direction with an offset of 133 μm , creating a 25x25 sheet of unit cells. A centered circle with a diameter equal to the side length of the sheet was added and an anti-extruded cut was performed, making a disk with a diameter of 25 unit cells and a thickness of one unit cell. The sheet was repeated in the z-direction three times with an offset of 133 μm and an STL file was saved. The same process was repeated two more times with 35x35 and 45x45 sheets to create disks with diameters of 35 and 45 unit cells, respectively. The STL files were then sliced using Anycubic Photon Workshop V2 to create a Pwma file. In all cases, the models were rotated 90° in the x-axis and 45° in the y-axis to minimize the sections that were orthogonal to the build plate.

Sample Preparation

The photocurable resin (ANYCUBIC Basic Sensitive Resin; UV wavelength 405 nm) was used as received. An LCD-SLA 3D printer (ANYCUBIC Photon Mono 4K), which has a resolution of 35 μm in all directions, was used as directed by the manufacturer. The UV intensity was set to 100% while the duration of UV exposure was 40 seconds for the first 4 layers and 2 seconds for all other layers. The retraction velocity of the build plate was set to 4 mm sec⁻¹. The 3D-printed resin microlattices were immediately immersed in ethanol for at least 3 hours to remove the uncured resin residue inside of the microstructure, then dried under ambient conditions overnight.

The dried resin microlattices were placed on a ceramic boat and loaded into a quartz tube furnace for two-step carbonization. The printed material was first pyrolyzed at 400°C for four hours to stabilize the material, then further pyrolyzed at 900°C for four hours to completely carbonize the material. A ramp rate of 5°C min⁻¹ and an N₂ environment were used throughout this process.

To deposit the FeS₂ on the surface of the carbonized materials, 233 mg of ferrocene (TGI, 98%) and 100 mg of sulfur (Alfa Aesar, 99.8%) were well mixed and ground with a mortar and pestle. The carbonized microlattice was then encapsulated by the well-mixed powder and wrapped in aluminum foil. The mixture was annealed at 500°C for 2 hours in a flowing N₂ atmosphere at a ramp rate of 5°C min⁻¹ to obtain the final FeS₂@Carbon samples. In cases where the blank carbon template was used and analyzed, the FeS₂ synthetic procedure stopped prior to the annealing step.

Structural Characterization

The crystal structure patterns were determined by recording diffraction patterns of the samples using an X-ray diffractometer (Rigaku D/Max2500) with Cu K α X-ray sources at a scanning speed of 3° min⁻¹ in a 2 θ range of 20°-70°. To further determine the elemental composition and chemical and electronic state of the material, X-ray photoelectron spectroscopy (XPS) measurements were performed with an Al K α X-ray source. The morphological analysis of the FeS₂@Carbon was performed by using a Thermo Scientific™ Apreo scanning electron microscope (SEM). To examine the properties of carbon as well as further affirm the presence of FeS₂ on the material, Raman spectroscopy was used. Micromeritics ASAP 2020 was used to determine the Brunauer-Emmett-Teller (BET) surface areas using the standard N₂ adsorption and desorption isotherm measurements at 77 K.

Battery Preparation and Electrochemical Measurements

The obtained FeS₂@Carbon disks were placed in an argon-filled glove box overnight, and then used to serve as electrodes for half-cell lithium-ion batteries. The electrochemical performance of the electrodes was investigated by using CR2032 coin cells with lithium metal foil as the counter and reference electrode. Celgard 2400 was used as the separator. LiPF₆ (1 M) in a mixture of ethylene carbonate/dimethyl carbonate/diethyl carbonate (EC/DMC/DEC; 1:1:1 in volume) solution was used as the electrolyte. Assembly of the coin cells took place inside the argon-filled glove box to keep oxygen and water content less than 1 ppm. Cyclic voltammetry was measured with a STAT III electrochemical workstation (Princeton Applied Research, USA) at a scan rate of 0.1, 0.2, 0.4, 0.6, 0.8, and 1.0 mV s⁻¹ in the voltage window of 0.05-3 V versus lithium (vs. Li⁺/Li). The galvanostatic charge/discharge measurements were performed by using a Landt battery testing system in the voltage window of 0.05-3 V versus lithium (vs. Li⁺/Li). The electrochemical impedance spectroscopy (EIS) measurements were conducted both before the cycling began and after 3 and 100 cycles, all at room temperature in a range of 1,000,000 Hz to 0.1 Hz. The specific capacity of FeS₂@Carbon can be calculated according to the Equations (1) and (2).

Equations:

$$\text{Gravimetric capacity (mAh g}^{-1}\text{)} = \frac{\text{capacity (mAh)}}{\text{mass after deposition (g)} - \text{mass before deposition(g)}} \quad (1)$$

$$\text{Areal capacity (mAh cm}^{-2}\text{)} = \frac{\text{capacity (mAh)}}{\text{Area of disk (cm}^2\text{)}} \quad (2)$$

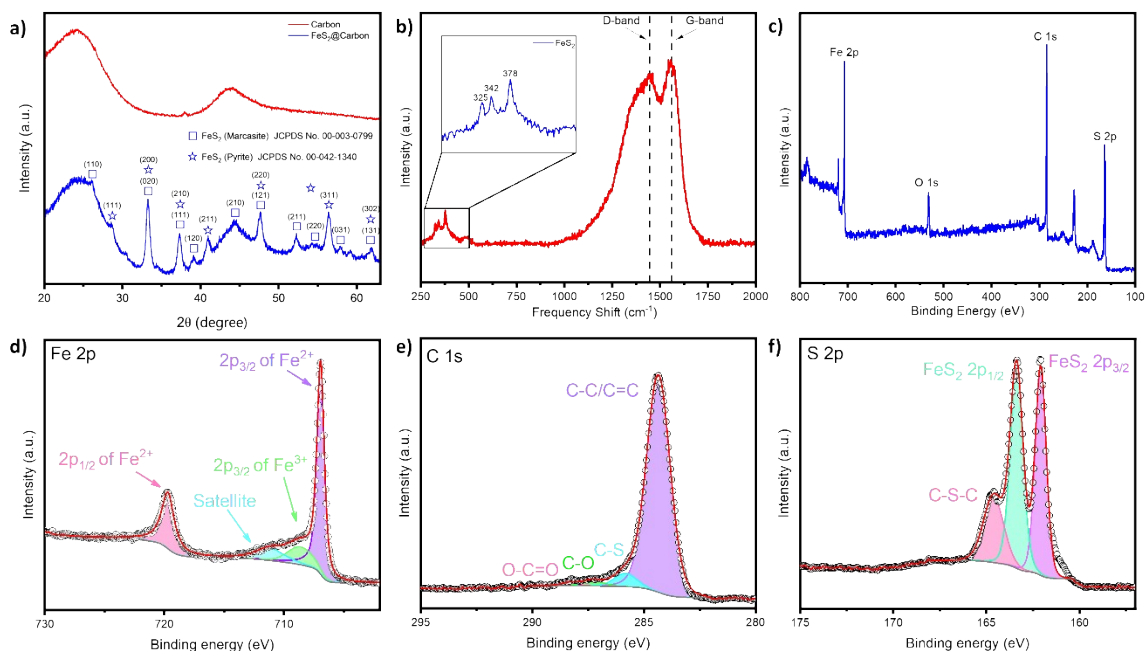


Figure S1 (a) XRD pattern of Carbon and FeS₂@Carbon; (b) Raman spectra of the FeS₂@Carbon; (c) XPS survey spectra; and (d-f) high-resolution XPS spectra of Fe 2p, C 1s, and S 2p of the as-obtained FeS₂@Carbon material, respectively.

As shown in Figure S1a, the carbon template samples exhibited two broad peaks around 25° and 45°, which have been well documented within the literature as carbon derived from epoxy resins.^{1, 2} The FeS₂@Carbon sample demonstrated eight total peaks, three of which are located at 2θ values of 37.29°, 44.44°, and 57.88° and correspond to the planes of (120), (211), and (031) of the Marcasite (orthorhombic) FeS₂ phase, respectively (JCPDS no. 00-003-0799). The last five peaks are located at 2θ values of 33.25°, 37.29°, 40.93°, 47.59°, and 56.40° and correspond to the planes of (200), (210), (211), (220), and (311) of the Pyrite (isometric) FeS₂ phase, respectively (JCPDS no. 00-042-1340). It is noted that the percent estimate for the Pyrite and Marcasite phases was 80wt% and 20wt%, respectively. All the peaks in the XRD patterns can be indexed to fully describe the material for both the carbon templates as well as the FeS₂@Carbon samples. In the Raman

spectra (Figure S1b), two prominent peaks are displayed at 1446.02 and 1556.20 cm^{-1} , which represent disordered carbon (D band) and sp^2 -hybridized graphitic carbon (G band), respectively.³ Meanwhile, another three peaks (inset of Figure S1b) are located at 325, 342, and 378 cm^{-1} , which shows the occurrence of iron disulfide, E_g (S_2 vibration)³, and A_g (S-S in phase stretch) of FeS_2 crystals, respectively, further indicating the successful formation of the $\text{FeS}_2@$ Carbon material.⁴

The full survey spectra of the $\text{FeS}_2@$ Carbon are shown in Figure S1c where Fe 2p, O 1s, C 1s, and S 2p can be identified. The presence of the O 1s peak could be originated from the printing resin or surface oxygen absorption when exposed to air during sample transfer. The Fe 2p XPS spectrum can be deconvoluted into four peaks (Figure S1d). Noticeably, the peaks located at 719.8 eV and 707.0 eV can be associated with the characteristic signal of $2p_{1/2}$ of Fe^{2+} and $2p_{3/2}$ of Fe^{2+} , respectively. Furthermore, the broad peak centralized around 708.1 eV corresponds to $2p_{3/2}$ of Fe^{3+} , meanwhile, the peak at 713.5 eV was aligned to the satellite peak, confirming the successful sulfurization process to form $\text{FeS}_2@$ Carbon.⁵⁻⁷ Figure S1e shows the C 1s can be deconvoluted into four peaks. The resolved C 1s spectrum of $\text{FeS}_2@$ Carbon shows the presence of four components: C-C/C=C (284.4 eV), C-S (285.8), C-O (287.3 eV), and O=C-O (288.4 eV). Lastly, the S 2p spectra (Figure S1f) is composed of three peaks. The peaks at 162.1 eV and 163.4 eV can be ascribed to the FeS_2 $2P_{3/2}$ and FeS_2 $2P_{1/2}$, respectively, further confirming the formation of FeS_2 on the surface. The third peak at 164.6 eV can be attributed to the C-S-C, substantiating the claim that there is some level of covalent bonding between the sulfur and carbon.^{5, 8-10}

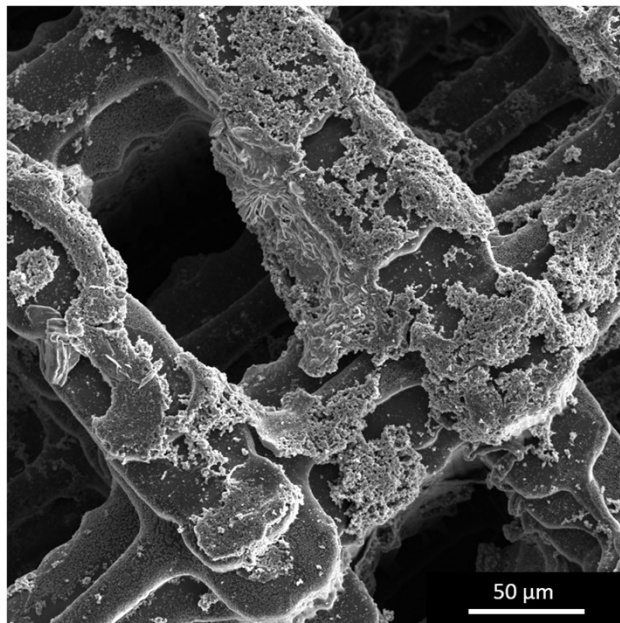


Figure S2 Cross-sectional image of the FeS₂@Carbon composite material.

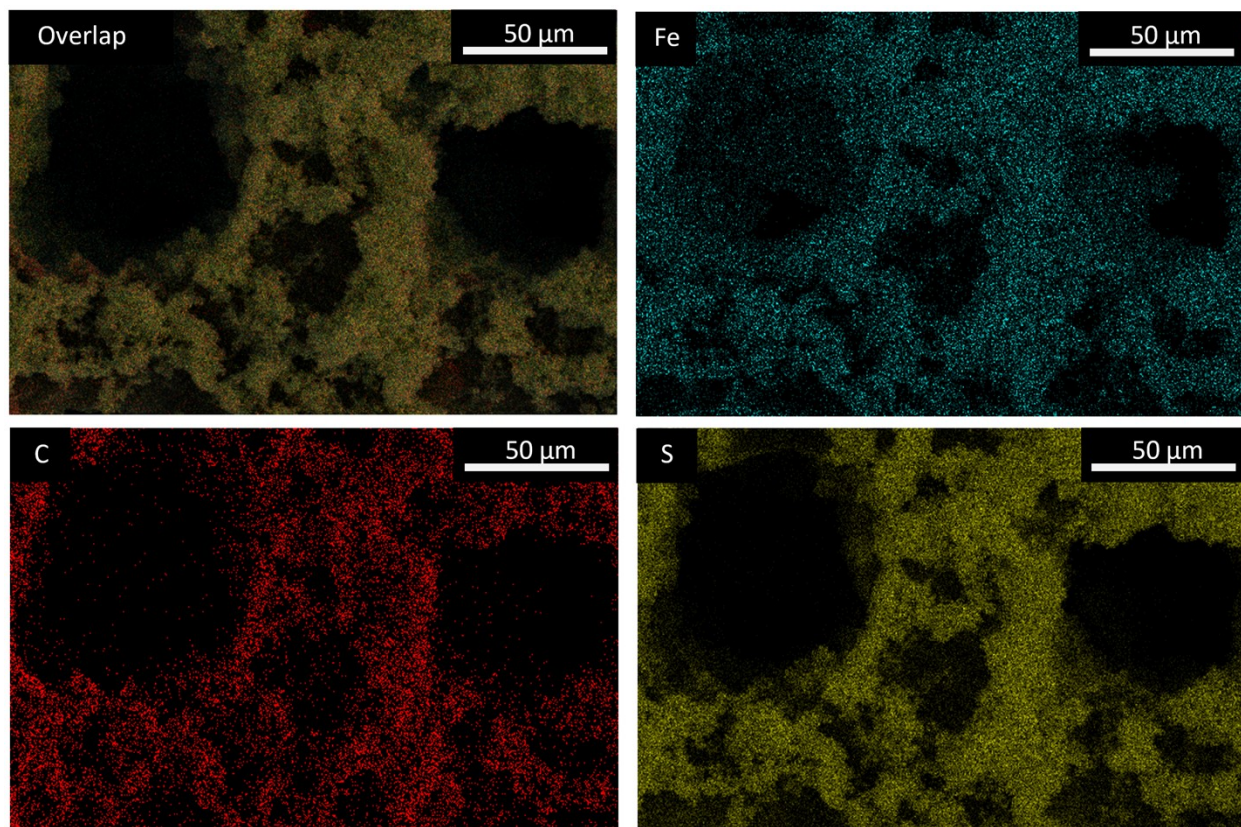


Figure S3 EDX mapping overlay, individual EDS elemental mapping of iron (blue) carbon (red) sulfur (yellow) for FeS₂@Carbon composite.

EDX was performed (Figure S3), showing that iron sulfide is well dispersed. Notice that the ferrocene's sandwich structure will also contribute to carbon after thermal treatment, which means the FeS₂ sphere is inherently enveloped in carbon thin layer, further enhancing the structural stability and conductivity.

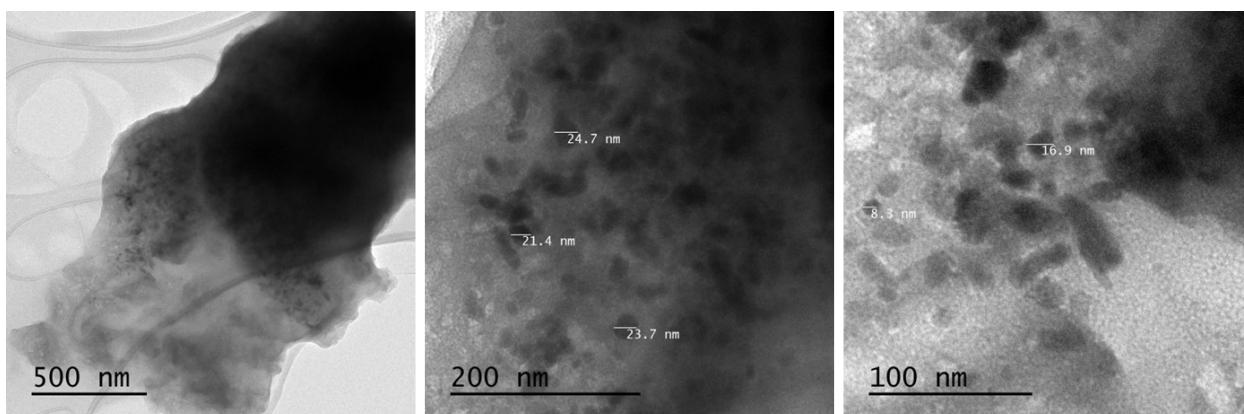


Figure S4 TEM imaging of FeS₂ at 500, 200, and 100 nm scale.

To clarify the structure and morphology of individual FeS₂ particles in the composite material, TEM imaging was performed. As can be seen in Figure S4, the particle size ranged from 8.3 to 24.9 nm. The particles are well enveloped by carbon derived from the cyclopentadiene rings, increasing robustness and conductivity.

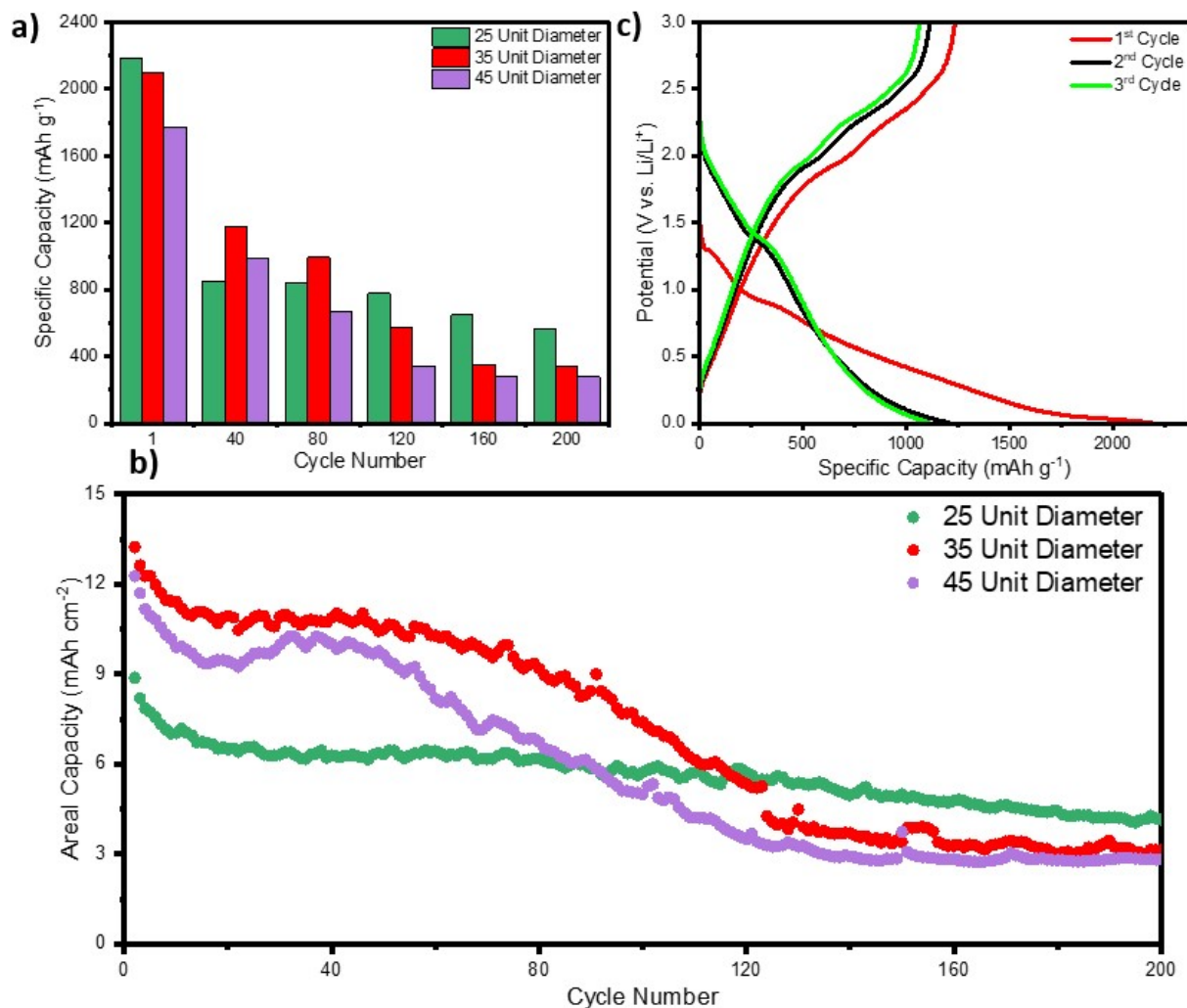


Figure S5 (a) Specific Capacity of 25, 35, and 45 diameter disks at various cycle numbers; (b) areal capacity of 25, 35, and 45 diameter disks up to 200 cycles at 12.5 mA cm⁻²; (c) galvanostatic charge-discharge profile of the FeS₂@Carbon electrode at 500 mA g⁻¹.

As depicted in Figure S5a, all three sizes exhibited a common trend: a significant drop off in specific capacity between the first cycle and subsequent cycles, primarily attributable to the formation of the solid electrolyte interphase (SEI).^{1, 11, 12} However, as the cycling continued beyond the 80th cycle, an intriguing shift emerged. Initially, the 35 unit diameter disk displayed the most favorable performance characteristics, outperforming the others. Yet, as we extended our analysis out to the 200th cycle, the 25 unit diameter emerged as the standout performer. This shift in performance is because larger templates allow for more active material, which leads to higher current at the same current density. Instead of the capacity of the battery scaling linearly with current density, the capacity follows Peukert's law, which states that as discharge increases, the available capacity decreases^{13, 14}. Furthermore, larger 3D printed materials may exhibit an increased likelihood of defects within the prints, potentially causing structural alterations over time that could impact their electrochemical performance¹⁵. The areal capacity of different size electrode disks is displayed in Figure S5b. It is found that after 200 cycles, the areal capacity of the 25, 35, and 45 unit diameter disks were 4.14 mAh cm⁻², 3.13 mAh cm⁻², and 2.82 mAh cm⁻², respectively. Since the 25 unit diameter disk displayed the best overall cycling stability from both a mass perspective as well as areal, it will be the primary focus moving forward as this proof-of-concept study on 3D printed electrodes. Figure S5c presents the galvanostatic charge/discharge profile of the FeS₂@Carbon samples at a current density of 500 mA g⁻¹. The profile shows a high initial discharge capacity of 2183 mAh g⁻¹ with an initial Coulombic Efficiency (CE) of 56.58%. This mediocre initial CE is due to the formation of the SEI layers that lead to irreversible consumption of lithium ions. After the first cycle, there is no significant decrease of capacity from the second to third cycle, suggesting good reversibility after the initial irreversible capacity loss. This claim is confirmed when looking at the CE, which begins to jump up to 92.56% and 95.69%

for the 2nd and 3rd cycles, respectively, and achieves a Coulombic Efficiency of more than 99% after ten cycles.

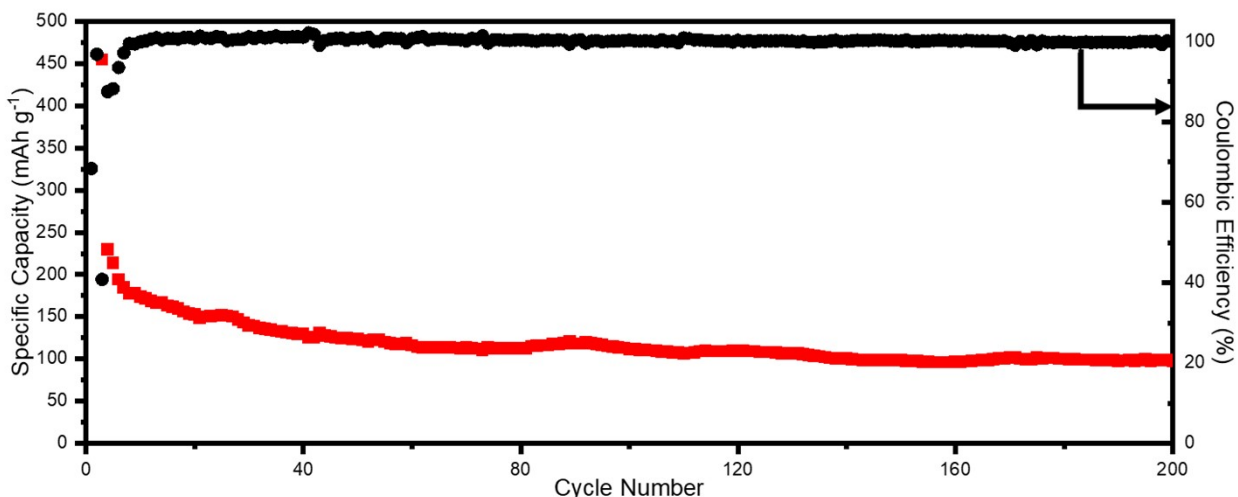


Figure S6 Cycling stability and Coulombic Efficiency for a 25 unit diameter disk over 200 cycles at 1 A g⁻¹ (formation not depicted).

As can be seen in Figure S6, the Coulombic efficiency was >99.5% after 10 cycles, the cell had a specific capacity of 97.7 mAh g⁻¹ after 200 cycles at 1 A g⁻¹, which is much lower than what was seen at 500 mA g⁻¹. This shows that the material struggles to maintain capacity at the higher current density, which could be improved with more research and development optimization. The potential solution is to embed FeS₂ into the carbon lattice to further enhance stability. In the current project, FeS₂ is only on the surface of the carbon lattice to demonstrate the concept. Surface particles have a high potential to fall off or pulverize during large current density cycling due to volume expansion.

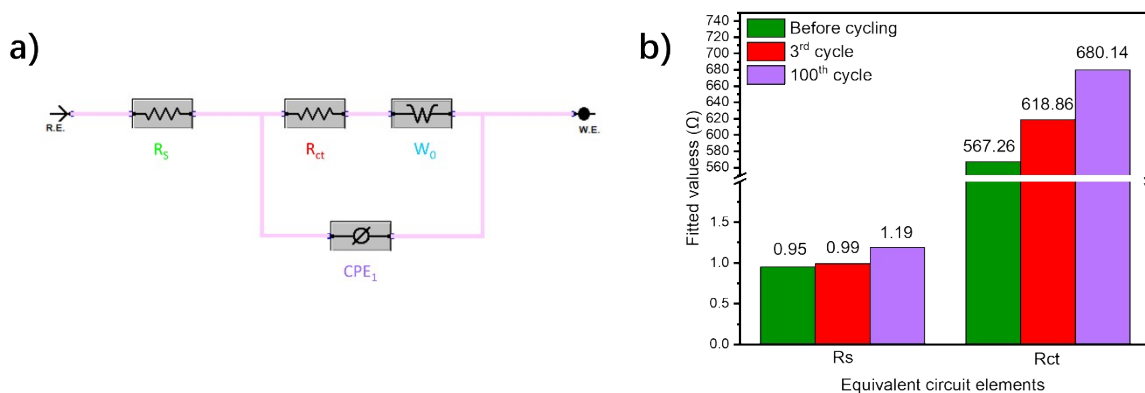


Figure S7 (a) The Equivalent circuit model; (b) The fitted values for the equivalent circuit elements.

The EIS data was meticulously fitted by employing the equivalent circuit, as depicted in Figure S7a, serving as a pivotal tool for the analysis. CPE1 corresponds to the constant phase element linked to the charge transfer resistance, while W_o relates to the Warburg impedance. The R_{ct} value of the $FeS_2@Carbon$ electrode prior to cycling, as graphically represented in Figure S7b, was discerned to be 567.26 Ω . Remarkably, this value was found to be lower than that of the $FeS_2@Carbon$ electrode after 3 cycles, and after 100 cycles which, in contrast, recorded a value of 618.86 Ω and 680.14 Ω .

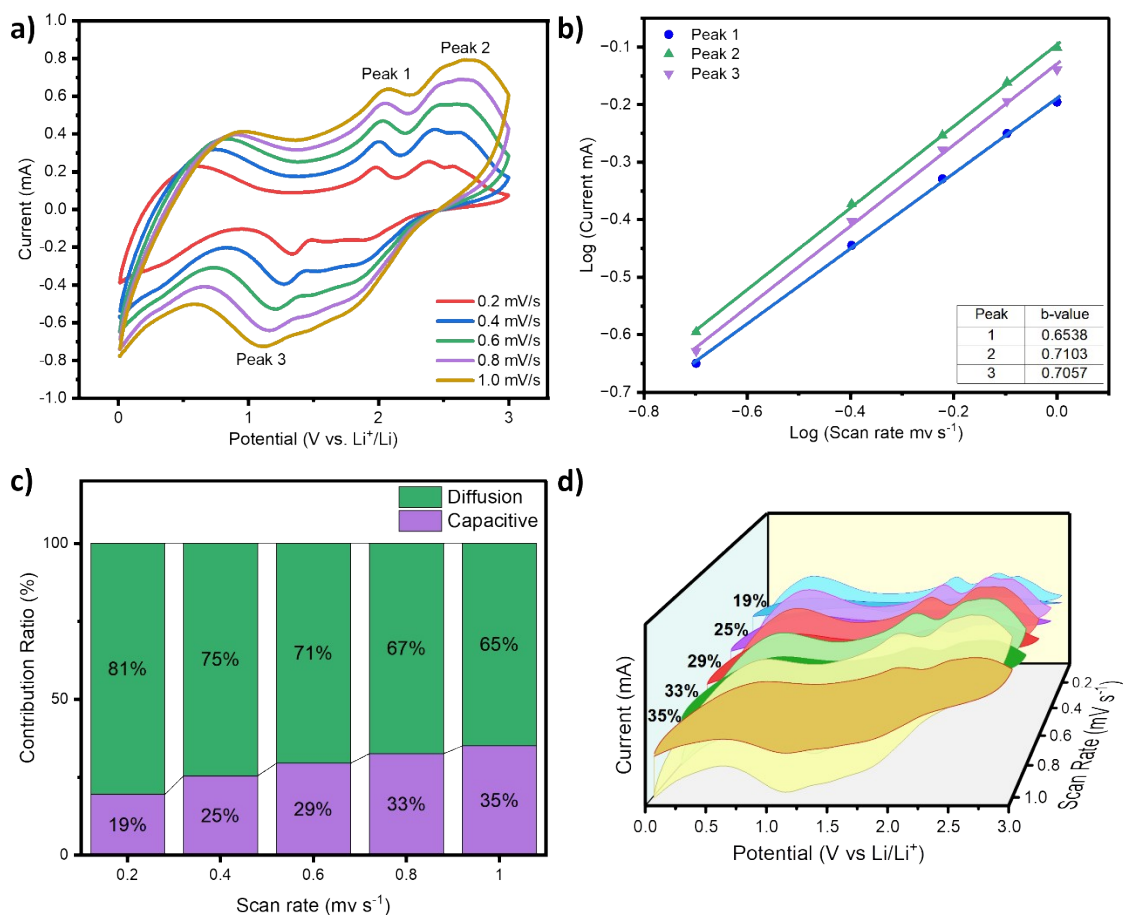


Figure S8 (a) CV curves of the cell at different scan rates after ten cycles; (b) the fitted lines of $\ln(\text{peak current})$ versus $\ln(\text{scan rate})$; (c) the pseudo-capacitance contribution at different scan rates; (d) CV curves and contribution ratios of the capacitive of FeS₂@Carbon electrode charge versus scan rate.

As shown in Figure S8a, the peak current density increased with the increasing scan rate, but the overall shape of the graph remained the same, indicating good kinetic reversibility of the material. To find a mechanistic relationship between the peak current (i) and scan rate (ν), the following equation can be used:¹⁶

$$i = a\nu^b \quad (3)$$

where a and b are the adjustable parameters. For the analysis, the b -value in the equation is a factor determining the type of charge storage mechanism in the electrode, for which there are generally two well-defined conditions, $b = 0.5$ and $b = 1.0$. A b value of 0.5 indicates a diffusion-controlled process whereas a b value of 1.0 indicates capacitive behavior. The area in between these values is known as the “transitional” area, which demonstrates a ratio of both diffusion and capacity control.¹⁶

In order to evaluate the adjustable parameters, Equation 3 can be converted to the following:

$$\log(i) = b \log(v) + \log\left(\frac{i_0}{a}\right) \quad (4)$$

where the b -value can be calculated from the slope of $\log(i)$ versus $\log(v)$. Figure S8b shows that the b -value for peaks 1-3 are 0.6538, 0.7103, and 0.7057, respectively. Since the slope values are closer to 0.5 than they are to 1.0, this indicates that the charge storage primarily resulted from a diffusion-controlled processes. Moreover, as a quantitative analysis of the capacitive and diffusion contributions of the electrode material, the Dunn Method can be used:^{16, 17}

$$i(v) = k_1 v + k_2 v^{1/2} \quad (5)$$

where $i(v)$ is the total current at a fixed voltage potential which can be divided into two parts: the $k_1 v$ is considered as capacitive-controlled current and $k_2 v^{1/2}$ is attributed to diffusion-controlled current.^{16, 18} The results are shown in Figure S8c, where the percentage of pseudocapacitance to the capacity is 19% at a scan rate of 0.2 mV s⁻¹, 25% at 0.4 mV s⁻¹, 29% at 0.6 mV s⁻¹, 33% at 0.8 mV s⁻¹, and 35% at 1.0 mV s⁻¹. These findings further confirm a diffusion-controlled process, which can be ascribed to the well-ordered channels in the carbon microlattice being oriented along the thickness of the electrode, allowing for fast ion/electron diffusion within the material. A

graphical representation of these findings can be found in Figure S8d, where the dark, shaded region represents the capacitive contribution while the light, shaded region represents the diffusion contribution at varying scan rates.

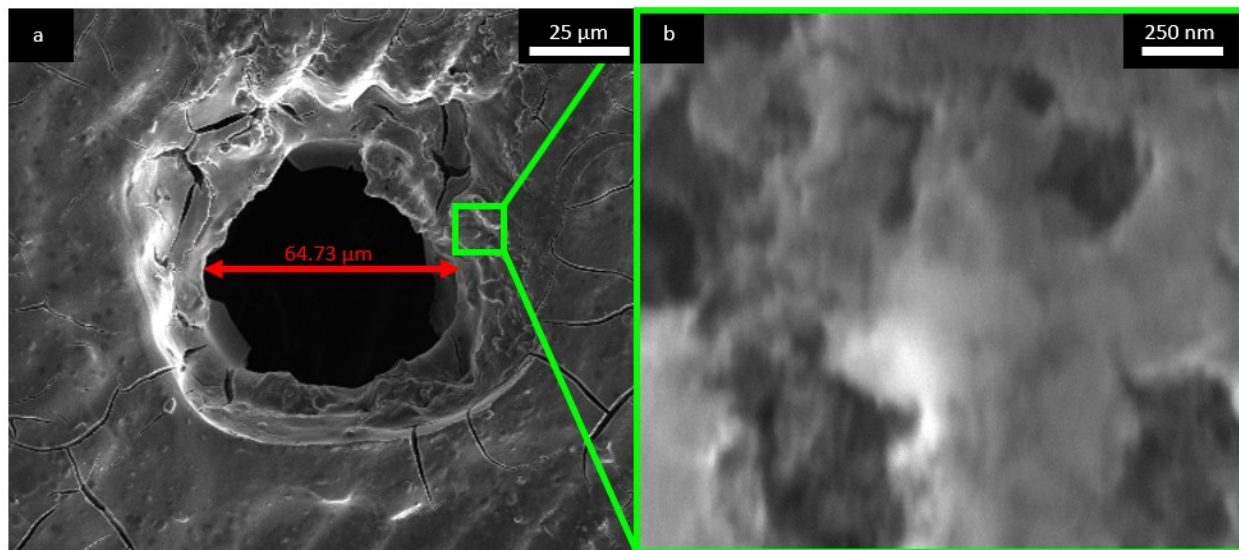


Figure S9 SEM images after 200 cycles of (a) one void of FeS₂@Carbon electrode; (b) High-magnification image of the sample

The FeS₂@Carbon demonstrated good cycling stability and rate capability in lithium-ion batteries. This promising electrochemical performance is attributed to the robust carbon microlattice templates and the utilization of the high-capacity material, FeS₂. For further evaluation of the electrode's structural stability, we disassembled a used coin cell in the glovebox and conducted imaging with SEM. As can be seen in Figure S9, the carbon microlattice still keeps its overall shape, without visible breakage or cracks. Furthermore, the void size shrunk down to approximately 64.73 μm after 200 cycles at a current density of 500 mA g⁻¹, which could be ascribed to the continuous formation of the SEI layer. Moreover, it is worth noting that the

electrolyte used in the battery could lead to the formation of salts on the surface after decrimping and drying, potentially contributing to the observed buildup.¹⁹

References

1. Y. Katsuyama, A. Kudo, H. Kobayashi, J. Han, M. Chen, I. Honma and R. B. Kaner, *Small*, 2022, **18**, 2202277.
2. Y. Katsuyama, N. Haba, H. Kobayashi, K. Iwase, A. Kudo, I. Honma and R. B. Kaner, *Advanced Functional Materials*, 2022, **32**, 2201544.
3. G. Chandrawat, J. Tripathi, A. Sharma, J. Singh and S. Tripathi, 2020.
4. L. Liu, Z. Yuan, C. Qiu and J. Liu, *Solid State Ionics*, 2013, **241**, 25-29.
5. L. Li, P. Ma, S. Hussain, L. Jia, D. Lin, X. Yin, Y. Lin, Z. Cheng and L. Wang, *Sustainable Energy & Fuels*, 2019, **3**, 1749-1756.
6. Z. Zeng, W. Li, X. Chen, N. Zhang, H. Qi and X. Liu, *ACS Sustainable Chemistry & Engineering*, 2020, **8**, 3261-3272.
7. G.-J. He, D.-J. Zhong, Y.-L. Xu, P. Liu, S.-J. Zeng and S. Wang, *Water, Air, & Soil Pollution*, 2021, **232**, 1-15.
8. A. Ghahremaninezhad, D. Dixon and E. Asselin, *Electrochimica Acta*, 2013, **87**, 97-112.
9. Y. Gao, Z. Li, Z. Fu, H. Zhang, G. Wang and H. Zhou, *Separation and Purification Technology*, 2021, **262**, 118336.
10. K. Chen, G. Li, Y. Wang, W. Chen and L. Mi, *Green Energy & Environment*, 2020, **5**, 50-58.
11. J. Li, J. Fleetwood, W. B. Hawley and W. Kays, *Chemical Reviews*, 2021, **122**, 903-956.
12. Z. Zhao, M. Sun, W. Chen, Y. Liu, L. Zhang, N. Dongfang, Y. Ruan, J. Zhang, P. Wang and L. Dong, *Advanced Functional Materials*, 2019, **29**, 1809196.
13. S. Hwang, D. Lee, Y. Rho, K. S. Yoon, D. M. Yu, S. J. Yoon, S. Kim, Y. T. Hong and S. So, *Journal of Power Sources*, 2021, **489**, 229497.
14. H. Cheng, R. Xiao, H. Bian, Z. Li, Y. Zhan, C. K. Tsang, C. Chung, Z. Lu and Y. Y. Li, *Materials Chemistry and Physics*, 2014, **144**, 25-30.
15. T. D. Ngo, A. Kashani, G. Imbalzano, K. T. Nguyen and D. Hui, *Composites Part B: Engineering*, 2018, **143**, 172-196.
16. I. E. Rauda, V. Augustyn, B. Dunn and S. H. Tolbert, *Accounts of chemical research*, 2013, **46**, 1113-1124.
17. A. G. Dylla, G. Henkelman and K. J. Stevenson, *Accounts of chemical research*, 2013, **46**, 1104-1112.
18. J. B. Cook, H. S. Kim, Y. Yan, J. S. Ko, S. Robbennolt, B. Dunn and S. H. Tolbert, *Advanced Energy Materials*, 2016, **6**, 1501937.
19. B. S. Parimalam and B. L. Lucht, *Journal of The Electrochemical Society*, 2018, **165**, A251.